J. Fluid Mech. (2019), *vol.* 874, *pp.* 339–358. © Cambridge University Press 2019
doi:10.1017/jfm.2019.457

Optimal viscous damping of vibrating porous cylinders

Saeed Jafari Kang[1], Esmaeil Dehdashti[1], Vahid Vandadi[2] and Hassan Masoud[1,†]

[1]Department of Mechanical Engineering–Engineering Mechanics, Michigan Technological University, Houghton, MI 49931, USA

[2]Polaris Industries Inc., Medina, MN 55340, USA

(Received 25 January 2019; revised 30 May 2019; accepted 1 June 2019;
first published online 9 July 2019)

We theoretically study small-amplitude oscillations of permeable cylinders immersed in an unbounded fluid. Specifically, we examine the effects of oscillation frequency, permeability and shape on the effective mass and damping coefficients, the latter of which is proportional to the power required to sustain the vibrations. Cylinders of circular and elliptical cross-sections undergoing transverse and rotational vibrations are considered. The dynamics of the fluid flow through porous cylinders is assumed to obey the unsteady Brinkman–Debye–Bueche equations. We use a singularity method to analytically calculate the flow field within and around circular cylinders, whereas we introduce a Fourier-pseudospectral method to numerically solve the governing equations for elliptical cylinders. We find that, if rescaled properly, the analytical results for circular cylinders provide very good estimates for the behaviour of elliptical ones over a wide range of conditions. More importantly, our calculations indicate that, at sufficiently high frequencies, the damping coefficient of oscillations varies non-monotonically with the permeability, in which case it maximizes when the diffusion length scale for the vorticity is comparable to the penetration length scale for the flow within the porous material. Depending on the oscillation period, the maximum damping of a permeable cylinder can be many times greater than that of an otherwise impermeable one. This might seem counter-intuitive at first, since generally the power it takes to steadily drag a permeable object through a fluid is less than the power needed to drive the steady motion of the same, but impermeable, object. However, the driving power (or damping coefficient) for oscillating bodies is determined not only by the amplitude of the cyclic fluid load experienced by them but also by the phase shift between the load and their periodic motion. An increase in the latter is responsible for the excess damping coefficient of vibrating porous cylinders.

Key words: flow–structure interactions, particle/fluid flow, porous media

1. Introduction

Over the years, various motivations have prompted researchers to investigate the dynamic response of fluid-submerged oscillating objects. A prominent example is

† Email address for correspondence: hmasoud@mtu.edu

the theoretical work of Stokes (1851) in the mid-nineteenth century on the vibration of a sphere in an unbounded fluid inspired by the motion of a simple pendulum performing indefinitely small oscillations in air. Since then, there have been a number of theoretical investigations focusing on the hydrodynamics of vibrating impermeable particles of different geometries (Ray 1936; Kanwal 1955, 1964, 1970; Williams 1966; Tuck 1969; Lai & Mockros 1972; Lawrence & Weinbaum 1986, 1988; Pozrikidis 1989; Loewenberg 1993; Avudainayagam & Geetha 1994; Zhang & Stone 1998; Shu & Chwang 2001; Shatz 2004, 2005; Barta 2011). These studies are motivated by applications ranging from the Brownian motion of microparticles and locomotion of microorganisms to frequency response of cantilever beams used in atomic force microscopes and design of bio-inspired swimming and flying robots.

A closer inspection of the literature indicates that oscillating motions of permeable objects, compared to those of their impermeable counterparts, remain largely unexplored. This is despite their importance in many conventional and emerging applications, such as the design of stabilizers for offshore structures (Molin 2001), enhanced oil recovery (Graham & Higdon 2002), oscillatory rheology of porous-particle suspensions (Looker & Carnie 2004) and aerodynamics of insect flight (Santhanakrishnan *et al.* 2014). The existing studies, which almost all belong to the current millennium, have only focused on the heaving motion of perforated disks (Molin 2001, 2011; Liu *et al.* 2011; An & Faltinsen 2013) and translational vibrations of porous spheres and spherical shells (Looker & Carnie 2004; Vainshtein & Shapiro 2009; Tsai & Hsu 2010; Ollila, Ala-Nissila & Denniston 2012; Prakash, Raja Sekhar & Kohr 2012). A missing elementary geometry in these investigations is a cylinder (be it circular or otherwise). Identifying the hydrodynamic characteristics of vibrating cylinders, however, has been shown to be the first step in understanding the behaviour of two-dimensional-like flow structures that appear frequently in systems of current interest (Sader 1998; Phan, Aureli & Porfiri 2013; Ahsan & Aureli 2015).

Here, we examine the hydrodynamics of porous cylinders vibrating in an infinite fluid medium. We consider both transverse and rotational oscillations for circular and elliptical cross-sections. Assuming small-amplitude oscillations, the unsteady Brinkman–Debye–Bueche (BDB) and linearized Navier–Stokes (NS) equations are solved for the fluid flow within and around cylinders, respectively. For circular cylinders, analytical solutions are obtained using the method of fundamental solutions; while for cylinders with elliptical cross-sections, a Fourier-pseudospectral method is devised to numerically calculate the flow field. We present the results in terms of the total forces and torques exerted on the oscillating cylinder. In particular, we scrutinize the influence of oscillation frequency and permeability on the effective mass and damping coefficients that are closely associated with the conservative and dissipative components of the hydrodynamic load, respectively. The latter is proportional to the power required to drive the vibrations. Our calculations reveal that, when the oscillation frequency is high enough, there exists a permeability at which the power (or damping coefficient) is maximum. Perhaps surprisingly, the maximum power can be several times greater than the power expended during the oscillations of an otherwise impermeable cylinder.

Below, we first describe the problem statement and modelling strategy. Details of the analytical and numerical approaches are explained next, followed by a discussion of the results, including the applicability range of the small-amplitude assumption. A short summary and concluding remarks are given in the end and supplemental information is provided in appendices A and B.

2. Problem formulation and solutions

2.1. *Governing equations*

We consider an infinitely long porous cylinder of characteristic (cross-sectional) length scale a and permeability κ that undergoes sinusoidal oscillations with constant amplitude A and period T in an unbounded incompressible fluid of density ρ and viscosity μ. We assume that the cylinder is neutrally buoyant and the amplitude of oscillations compared to the characteristic length of the cylinder is very small, i.e. $\lambda = A/a \ll 1$. Also, following Brinkman (1947, 1948) and Debye & Bueche (1948), we model the flow through the porous cylinder by adding a term proportional to the relative velocity of the cylinder to the momentum equation. This approach leads to a set of unsteady BDB and linearized NS equations that can be written succinctly in the dimensionless form as (see e.g. Vainshtein & Shapiro 2009; Ollila *et al.* 2012)

$$\mathcal{R}\frac{\partial \tilde{\boldsymbol{u}}}{\partial \tilde{t}} = \nabla^2 \tilde{\boldsymbol{u}} - \boldsymbol{\nabla}\tilde{p} - \chi\beta^2(\tilde{\boldsymbol{u}} - \tilde{\boldsymbol{u}}_c), \tag{2.1a}$$

$$\boldsymbol{\nabla}\cdot\tilde{\boldsymbol{u}} = 0, \tag{2.1b}$$

where $\tilde{t}$ denotes the time, $\tilde{p}$ represents the pressure field, $\tilde{\boldsymbol{u}}$ and $\tilde{\boldsymbol{u}}_c$ are the fluid and cylinder velocities, respectively, and χ is a binary mask function that is one inside the cylinder and zero in its exterior. As intended, $\chi = 1$ and $\chi = 0$ give, respectively, the unsteady BDB and unsteady Stokes equations that are coupled through the continuity of velocity and traction vector at the surface of the cylinder. The fluid velocity within the porous region is an averaged quantity over a domain that is large compared to the size of a single pore, but small compared to the cylinder itself. Furthermore, $\tilde{\boldsymbol{u}}$ is assumed to vanish at infinity. In (2.1),

$$\mathcal{R} = \rho\varpi a^2/\mu \quad \text{and} \quad \beta^2 = a^2/\kappa \tag{2.2a,b}$$

denote, respectively, the dimensionless frequency and permeability, with $\varpi = 2\pi/T$ being the angular frequency of the oscillations. The parameter $\mathcal{R}$ is also known as the oscillatory Reynolds number Re_ϖ. As we will discuss later in § 3, the values of $\mathcal{R}$ and β determine how fast the oscillations of the surrounding fluid decay as the distance from the cylinder increases and how deep the fluid flow penetrates into the porous cylinder, respectively. The ratio

$$\delta = \beta/\sqrt{\mathcal{R}} \tag{2.3}$$

will be shown to be an important factor in characterizing the hydrodynamic response of the vibrating cylinder. Throughout the article, the length, time, velocity, stress, force per unit length and torque per unit length are non-dimensionalized by a, $1/\varpi$, $A\varpi$, $\mu A\varpi/a$, $\mu A\varpi$ and $\mu aA\varpi$, respectively.

Given the form of the cylinder motion, it is mathematically convenient to express the velocities and pressure as real parts of complex quantities, i.e. $\tilde{\boldsymbol{u}}_c = \mathrm{Re}(\boldsymbol{u}_c e^{i\tilde{t}})$, $\tilde{\boldsymbol{u}} = \mathrm{Re}(\boldsymbol{u}e^{i\tilde{t}})$ and $\tilde{p} = \mathrm{Re}(pe^{i\tilde{t}})$, with $i^2 = -1$. Substituting in (2.1), we then have

$$\nabla^2\boldsymbol{u} - \boldsymbol{\nabla}p = \xi_i^2[\boldsymbol{u} - (\beta/\xi_i)^2\boldsymbol{u}_c] \quad \text{when } \chi = 1, \tag{2.4a}$$

$$\nabla^2\boldsymbol{u} - \boldsymbol{\nabla}p = \xi_o^2\boldsymbol{u} \quad \text{when } \chi = 0, \tag{2.4b}$$

$$\boldsymbol{\nabla}\cdot\boldsymbol{u} = 0, \tag{2.4c}$$

where

$$\xi_i^2 = i\mathcal{R} + \beta^2 \quad \text{and} \quad \xi_o^2 = i\mathcal{R}. \tag{2.5a,b}$$

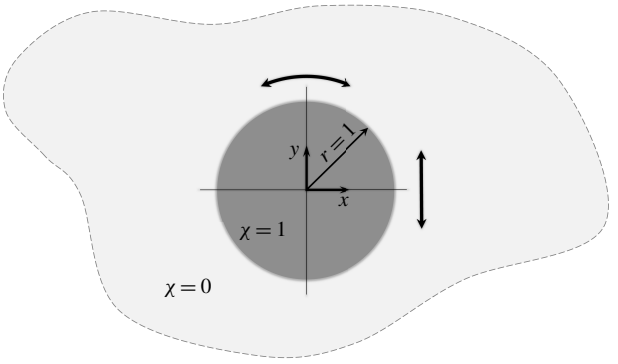

FIGURE 1. Schematic of a vibrating cylinder (depicted as a dark grey circle of dimensionless radius one) immersed in a boundless fluid (shown in light grey). The dashed enclosing contour highlights the lack of an outer boundary, and $\chi = 0$ and $\chi = 1$ denote areas inside and outside of the cylinder, respectively. Also, double-headed arrows represent transverse and rotational vibrations.

Here and throughout the article, we recognize the applicability domain of parameters and variables, being inside or outside the cylinder, by subscripts i and o, respectively. The time-independent equations (2.4*a*) and (2.4*b*) are in the form of the original BDB equations with complex dimensionless permeabilities. In solving (2.4), we treat circular and non-circular cross-sections separately, as only the former is amenable to analytical solutions.

2.2. *Analytical solutions for circular cylinders*

A convectional approach to analytically calculate $\boldsymbol{u}$ for simple geometries, such as spheres and circular cylinders, is to write (2.4) in terms of the streamfunction and solve the corresponding equations by the method of separation of variables. This method is used by Vainshtein & Shapiro (2009) and Ollila *et al.* (2012) to obtain the velocity and pressure fields for an oscillating sphere. Alternatively, here, we solve (2.4) for a circular cylinder of radius a (see figure 1) via the method of fundamental solutions. In this approach, $\boldsymbol{u} - (\beta/\xi_i)^2\boldsymbol{u}_c$ when $\chi = 1$ and $\boldsymbol{u}$ when $\chi = 0$ are represented, respectively, by the solutions of the homogeneous part of (2.4*a*) and (2.4*b*) that are in turn singular at infinity and the centre of the cylinder. The fundamental singular solutions necessary for representing the flow within and around the cylinder are analogues of stokeson, potential doubleton and roton for internal, and stokeslet, potential doublet and rotlet for external Stokes flows. The terminologies are adopted from those of Chwang & Wu (1975) and Pozrikidis (1992).

Let the subscripts *SN*, *DN* and *RN* denote the field variables for the equivalents of stokeson, potential doubleton and roton, respectively. Also, suppose analogues of stokeslet, potential doublet and rotlet are represented, respectively, by the subscripts *S*, *D* and *R*. Following this convention, we write the fundamental singularities of the BDB equations for internal and external flows as

$$\boldsymbol{u}_{SN}(\boldsymbol{r};\boldsymbol{\alpha}) = \left[\mathrm{I}_0(\rho_i) - \frac{\mathrm{I}_1(\rho_i)}{\rho_i}\right]\boldsymbol{\alpha} - \left[\mathrm{I}_0(\rho_i) - \frac{2\mathrm{I}_1(\rho_i)}{\rho_i}\right]\frac{(\boldsymbol{\alpha}\cdot\boldsymbol{r})\boldsymbol{r}}{r^2}, \tag{2.6a}$$

$$p_{SN}(\boldsymbol{r};\boldsymbol{\alpha}) = 0, \tag{2.6b}$$

$$\boldsymbol{u}_{DN}(\boldsymbol{r};\,\boldsymbol{\eta}) \;=\; \boldsymbol{\eta}, \tag{2.7a}$$
$$p_{DN}(\boldsymbol{r};\,\boldsymbol{\eta}) \;=\; -\xi_i^2(\boldsymbol{\eta}\cdot\boldsymbol{r}), \tag{2.7b}$$

$$\boldsymbol{u}_{RN}(\boldsymbol{r};\,\boldsymbol{\gamma}) \;=\; \frac{\mathrm{I}_1(\rho_i)}{\rho_i}(\boldsymbol{\gamma}\times\boldsymbol{r}), \tag{2.8a}$$
$$p_{RN}(\boldsymbol{r};\,\boldsymbol{\gamma}) \;=\; 0, \tag{2.8b}$$

$$\boldsymbol{u}_S(\boldsymbol{r};\,\boldsymbol{\alpha}) \;=\; \left[\mathrm{K}_0(\rho_o)+\frac{\mathrm{K}_1(\rho_o)}{\rho_o}-\frac{1}{\rho_o^2}\right]\boldsymbol{\alpha}-\left[\mathrm{K}_0(\rho_o)+\frac{2\mathrm{K}_1(\rho_o)}{\rho_o}-\frac{2}{\rho_o^2}\right]\frac{(\boldsymbol{\alpha}\cdot\boldsymbol{r})\boldsymbol{r}}{r^2}, \tag{2.9a}$$
$$p_S(\boldsymbol{r};\,\boldsymbol{\alpha}) \;=\; \frac{\boldsymbol{\alpha}\cdot\boldsymbol{r}}{r^2}, \tag{2.9b}$$

$$\boldsymbol{u}_D(\boldsymbol{r};\,\boldsymbol{\eta}) \;=\; -\frac{\xi_o^2}{2}\left\{\left[\mathrm{K}_0(\rho_o)+\frac{\mathrm{K}_1(\rho_o)}{\rho_o}\right]\boldsymbol{\eta}-\left[\mathrm{K}_0(\rho_o)+\frac{2\mathrm{K}_1(\rho_o)}{\rho_o}\right]\frac{(\boldsymbol{\eta}\cdot\boldsymbol{r})\boldsymbol{r}}{r^2}\right\}, \tag{2.10a}$$
$$p_D(\boldsymbol{r};\,\boldsymbol{\eta}) \;=\; 0, \tag{2.10b}$$

$$\boldsymbol{u}_R(\boldsymbol{r};\,\boldsymbol{\gamma}) \;=\; \xi_o^2\frac{\mathrm{K}_1(\rho_o)}{\rho_o}(\boldsymbol{\gamma}\times\boldsymbol{r}), \tag{2.11a}$$
$$p_R(\boldsymbol{r};\,\boldsymbol{\gamma}) \;=\; 0, \tag{2.11b}$$

where $\boldsymbol{r}$ is the position vector in the x–y plane with $|\boldsymbol{r}| = r = 1$ representing the surface of the cylinder, and I_n and K_n are modified Bessel functions of the first and second kinds and of order n, respectively (Abramowitz & Stegun 1972). Also, $\rho_i = \xi_i r$, $\rho_o = \xi_o r$ and $\boldsymbol{\alpha}$, $\boldsymbol{\beta}$ and $\boldsymbol{\gamma}$ are constant vectors reflecting the strength of the singular solutions. We note that $\boldsymbol{\alpha}$ and $\boldsymbol{\beta}$ lie in the x–y plane, to which $\boldsymbol{\gamma}$ is perpendicular. Equations (2.6*a*)–(2.11*b*) are derived in a similar fashion to their Stokes flow analogues (see e.g. Chwang & Wu 1975; Pozrikidis 1992).

We first consider the translational oscillations where, without loss of generality, we set $\boldsymbol{u}_c = \boldsymbol{e}_y$ with $\boldsymbol{e}_y$ being the unit vector in the y direction. In this case, we express the flow field as

$$\boldsymbol{u}_i \;=\; \boldsymbol{u}_{SN}(\boldsymbol{r};\,\alpha_i\boldsymbol{e}_y)+\boldsymbol{u}_{DN}(\boldsymbol{r};\,\eta_i\boldsymbol{e}_y)+(\beta/\xi_i)^2\boldsymbol{e}_y, \tag{2.12a}$$
$$p_i \;=\; p_{SN}(\boldsymbol{r};\,\alpha_i\boldsymbol{e}_y)+p_{DN}(\boldsymbol{r};\,\eta_i\boldsymbol{e}_y), \tag{2.12b}$$

$$\boldsymbol{u}_o \;=\; \boldsymbol{u}_S(\boldsymbol{r};\,\alpha_o\boldsymbol{e}_y)+\boldsymbol{u}_D(\boldsymbol{r};\,\eta_o\boldsymbol{e}_y), \tag{2.13a}$$
$$p_o \;=\; p_S(\boldsymbol{r};\,\alpha_o\boldsymbol{e}_y)+p_D(\boldsymbol{r};\,\eta_o\boldsymbol{e}_y), \tag{2.13b}$$

where the complex constants α_i, α_o, η_i and η_o are determined by applying, at $r = 1$,

$$\boldsymbol{u}_i = \boldsymbol{u}_o \quad\text{and}\quad \boldsymbol{n}\cdot\boldsymbol{\sigma}_i = \boldsymbol{n}\cdot\boldsymbol{\sigma}_o, \tag{2.14a,b}$$

with $\boldsymbol{\sigma}$ denoting the dimensionless (complex) stress tensor and $\boldsymbol{n} = \boldsymbol{e}_r = \boldsymbol{r}/r$. Given the first condition in (2.14) and recalling that $\nabla\cdot\boldsymbol{u} = 0$ everywhere, the continuity of the surface traction condition can be replaced by the continuity of pressure and vorticity $\boldsymbol{\omega} = \nabla\times\boldsymbol{u}$ (see e.g. Pozrikidis 2011, p. 241), i.e.

$$p_i = p_o \quad\text{and}\quad \boldsymbol{\omega}_i = \boldsymbol{\omega}_o. \tag{2.15a,b}$$

Note that, in two dimensions, the vorticity vector is effectively a scalar since it has only one non-zero component, which is normal to the x–y plane.

Substitution of (2.11) and (2.12) into the left-hand equation of (2.14) and the two equations of (2.15), yields, after some manipulations,

$$\alpha_i = \frac{A_3}{A_2}, \quad \eta_i = -\frac{A_1}{\xi_i^2 A_2}, \quad \alpha_o = \frac{A_1}{A_2}, \quad \eta_o = \frac{2(A_1 + A_4)}{\xi_o^2 A_2}, \tag{2.16a–d}$$

where

$$A_1 = [2\xi_o(\xi_i^2 - \xi_o^2)\mathrm{K}_1(\xi_o) + \xi_i^2\xi_o^2\mathrm{K}_0(\xi_o)]\mathrm{I}_1(\xi_i) + \xi_i\xi_o^3\mathrm{K}_1(\xi_o)\mathrm{I}_0(\xi_i), \tag{2.17a}$$

$$A_2 = \beta^{-2}\{[2\xi_o(\xi_i^2 - \xi_o^2)\mathrm{K}_1(\xi_o) + \xi_i^2(\xi_i^2 + \xi_o^2)\mathrm{K}_0(\xi_o)]\mathrm{I}_1(\xi_i) + \xi_i\xi_o(\xi_i^2 + \xi_o^2)\mathrm{K}_1(\xi_o)\mathrm{I}_0(\xi_i)\}, \tag{2.17b}$$

$$A_3 = -2\xi_i\xi_o\mathrm{K}_1(\xi_o), \tag{2.17c}$$

$$A_4 = -2\xi_i^2\mathrm{I}_1(\xi_i). \tag{2.17d}$$

The modified Bessel functions of complex argument can be evaluated using conventional mathematical software packages such as MATLAB and Mathematica, or independently using the definitions provided by Abramowitz & Stegun (1972). Having determined $\boldsymbol{u}$ and p in the entire domain, the (complex) total force per unit length of the cylinder is calculated as (see e.g. Felderhof 2014)

$$\boldsymbol{F} = \beta^2 \int_S (\boldsymbol{u}_i - \boldsymbol{u}_c)\,\mathrm{d}S = \frac{\pi\beta^2}{\xi_i^2}[\alpha_i\xi_i\mathrm{I}_1(\xi_i) + \eta_i\xi_i^2 - \mathrm{i}\mathcal{R}]\boldsymbol{e}_y. \tag{2.18}$$

The effective mass and damping coefficients are then obtained according to

$$C_e^t = -\mathrm{Im}[F/(\pi\mathcal{R})] \quad \text{and} \quad C_d^t = -\mathrm{Re}[F/(\pi\mathcal{R})], \tag{2.19a,b}$$

respectively, where $\boldsymbol{F} = F\boldsymbol{e}_y$ and the superscript t underscores transverse oscillations. We note that C_e^t represents both the inertia of the fluid mass within the porous cylinder and that of the surrounding fluid.

Next, we consider the rotational vibrations of a porous circular cylinder about its longitudinal axis. We set $A = a\Theta$ with Θ being the angular amplitude of oscillations. Consequently, $\boldsymbol{u}_c = \boldsymbol{e}_z \times \boldsymbol{r}$, where $\boldsymbol{e}_z$ is the unit vector in the z direction of the Cartesian coordinate system (x, y, z). Here, the internal and external flows take the forms of

$$\boldsymbol{u}_i = \boldsymbol{u}_{RN}(\boldsymbol{r}; \gamma_i\boldsymbol{e}_z) + (\beta/\xi_i)^2(\boldsymbol{e}_z \times \boldsymbol{r}), \tag{2.20a}$$

$$p_i = p_{RN}(\boldsymbol{r}; \gamma_i\boldsymbol{e}_z), \tag{2.20b}$$

$$\boldsymbol{u}_o = \boldsymbol{u}_R(\boldsymbol{r}; \gamma_o\boldsymbol{e}_z), \tag{2.21a}$$

$$p_o = p_R(\boldsymbol{r}; \gamma_o\boldsymbol{e}_z), \tag{2.21b}$$

where γ_i and γ_o are complex constants. Following the procedure that led to (2.16), the application of the continuity boundary conditions yields

$$\gamma_i = -\frac{\xi_o\beta^2\mathrm{K}_2(\xi_o)}{\xi_i[\xi_i\mathrm{I}_0(\xi_i)\mathrm{K}_1(\xi_o) + \xi_o\mathrm{I}_1(\xi_i)\mathrm{K}_0(\xi_o)]}, \tag{2.22a}$$

$$\gamma_o = \frac{\beta^2\mathrm{I}_2(\xi_i)}{\xi_i\xi_o[\xi_i\mathrm{I}_0(\xi_i)\mathrm{K}_1(\xi_o) + \xi_o\mathrm{I}_1(\xi_i)\mathrm{K}_0(\xi_o)]}, \tag{2.22b}$$

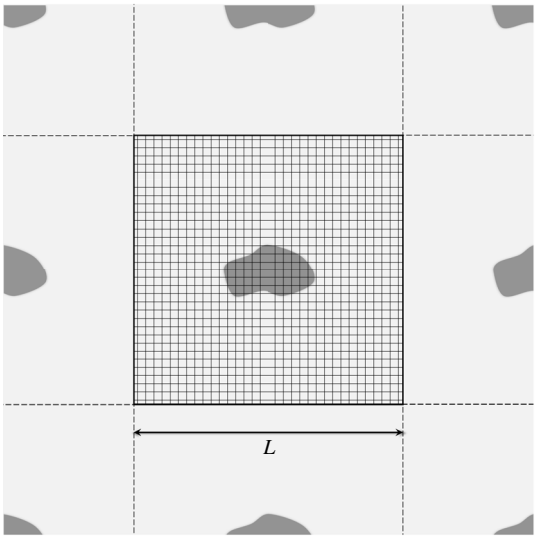

FIGURE 2. Schematic illustrating a periodic domain of length L (depicted as a thick black square) that is uniformly discretized into an array of square elements. The dark grey regions represent identical cylinders of non-circular cross-section that are spaced a domain length apart from one another.

which, in turn, results in the following equation for the total torque per unit length of the cylinder:

$$\boldsymbol{T} = \beta^2 \int_S [\boldsymbol{r} \times (\boldsymbol{u}_i - \boldsymbol{u}_c)]\,\mathrm{d}S = \frac{\pi\beta^2}{2\xi_i^2}[4\gamma_i \mathrm{I}_2(\xi_i) - \mathrm{i}\mathcal{R}]\boldsymbol{e}_z. \tag{2.23}$$

The effective mass and damping coefficients are derived from the complex torque as

$$C_e^r = -\mathrm{Im}[T/(\pi\mathcal{R}R_g^2)] \quad \text{and} \quad C_d^r = -\mathrm{Re}[T/(\pi\mathcal{R}R_g^2)], \tag{2.24a,b}$$

respectively, where R_g is the radius of gyration of the cross-section, defined as $R_g^2 = \int_S r^2\,\mathrm{d}S/\int_S \mathrm{d}S$, $\boldsymbol{T} = T\boldsymbol{e}_z$, and the superscript r denotes rotational oscillations.

2.3. *Numerical solutions for non-circular cylinders*

Obtaining closed-form solutions for $\boldsymbol{u}$ and p for cylinders of non-circular cross-sections is very challenging, if not impossible. Thus, we resort to numerics to study their dynamic response under transverse and rotational oscillations. To this end, we approximate the fluid flow within and around an isolated vibrating cylinder with that through and surrounding each member of a periodic array of oscillating cylinders (see figure 2). The latter is known to converge to the former as the spacing between the cylinders in the array becomes very large. We then employ a Fourier-pseudospectral method to calculate the velocity field and the resulting hydrodynamic loads.

We begin by taking the Fourier transform of (2.4), which, after rearranging, leads to

$$(k^2 + \xi_o^2)\hat{\boldsymbol{u}} + \mathrm{i}\boldsymbol{k}\hat{p} = -\beta^2(\widehat{\chi\boldsymbol{u}} - \widehat{\chi\boldsymbol{u}}_c) \quad \text{and} \quad \mathrm{i}\boldsymbol{k}\cdot\hat{\boldsymbol{u}} = 0, \tag{2.25a,b}$$

where $\boldsymbol{k}$ is the two-dimensional wavevector with $k = |\boldsymbol{k}|$ and the hat overbar denotes the transformed variables and terms. Taking the dot product of each side of the momentum equation in (2.25) by i$\boldsymbol{k}$ (i.e. taking the divergence), we find

$$\hat{p} = \beta^2 \frac{\mathrm{i}\boldsymbol{k}}{k^2} \cdot (\widehat{\chi \boldsymbol{u}} - \widehat{\chi \boldsymbol{u}}_c), \tag{2.26}$$

which, after substitution back into the momentum equation, results in

$$\boldsymbol{u} + \mathfrak{F}^{-1}\left\{\zeta\left[\widehat{\chi \boldsymbol{u}} - \frac{\boldsymbol{k}}{k^2}(\boldsymbol{k} \cdot \widehat{\chi \boldsymbol{u}})\right]\right\} = \mathfrak{F}^{-1}\left\{\zeta\left[\widehat{\chi \boldsymbol{u}}_c - \frac{\boldsymbol{k}}{k^2}(\boldsymbol{k} \cdot \widehat{\chi \boldsymbol{u}}_c)\right]\right\}, \tag{2.27}$$

where $\mathfrak{F}^{-1}$ represents the inverse Fourier transform and $\zeta = \beta^2/(k^2 + \xi_o^2)$.

To solve this equation numerically, we first discretize the periodic domain (see figure 2) into a uniform distribution of N square elements whose centres lie inside the domain boundary. Then, we enforce (2.27) at the centre of the elements (also known as the collocation points) while using a fast Fourier transform (FFT) to calculate the direct and inverse transforms. This gives rise to a set of linear equations for $\boldsymbol{u}$ at the centre of the grid cells, which can be solved iteratively via the generalized minimal residual method (GMRES). Note that in this approach the continuity boundary conditions at the surface of the cylinder are automatically satisfied since a single velocity field represents the entire flow. Finally, we calculate the total force and torque exerted on the cylinder using

$$\boldsymbol{F} = \beta^2 \sum_{j=1}^{N} S_j \chi_j (\boldsymbol{u}_j - \boldsymbol{u}_c), \tag{2.28a}$$

$$\boldsymbol{T} = \beta^2 \sum_{j=1}^{N} S_j \chi_j [\boldsymbol{r}_j \times (\boldsymbol{u}_j - \boldsymbol{u}_c)], \tag{2.28b}$$

where S_j, χ_j, $\boldsymbol{u}_j$ and $\boldsymbol{r}_j$ denote the surface area, value of the mask function, velocity and location of the centre of the jth element, respectively.

Throughout the calculations, we set the length of the periodic domain L and number of grid points such that always $20 \leqslant L/a$ and the size of the largest grid cell is smaller than $0.01a$. Recall that a is the characteristic length scale of the cross-section, e.g. the radius for circular and semi-major axis for elliptical cylinders. Further, the mask function is smoothed over five nodes by a Gaussian filter to avoid spurious Gibbs oscillations that usually appear when taking the FFT of discontinuous functions (see e.g. Kolomenskiy & Schneider 2009). We verify the accuracy of our numerical approach by comparing its results for circular cylinders with the analytical formulae of § 2.2, and find that the relative errors of the effective mass and damping coefficients for $0 < \beta \leqslant 10^2$ and $10^{-1} \leqslant \mathcal{R} \leqslant 10^3$ are less than 2.2 %. Extending the upper limits of β and $\mathcal{R}$ in numerical simulations requires finer grid resolutions, and reducing the lower limit of $\mathcal{R}$ demands larger periodic domains. It is worth noting that the limit of $\mathcal{R} \to 0$ is logarithmically singular for the case of transverse oscillations (see e.g. table 1 in appendix A), i.e. no steady-state solution exists for $\mathcal{R} = 0$.

The methodology explained above can be applied to any cross-sectional geometry (circular or otherwise), but here we focus only on ellipses due to their practical significance. Furthermore, this numerical approach can be extended to solve the coupled unsteady BDB–NS equations, including the nonlinear term we neglected

so far thanks to the small-amplitude assumption. In its most simple form, the vorticity–streamfunction formulation of the equations are first transformed into the Fourier space. Then, the nonlinear advective and permeability-dependent terms are treated explicitly (e.g. using a second-order Adams–Bashforth method), while the linear diffusive term is integrated exactly via the integrating factor technique (see e.g. Kolomenskiy & Schneider 2009). Note that the mask function is, in general, time-dependent and varies according to the position of the object, unless the equations are written in a non-inertial reference frame attached to the oscillating object. Here, we use the extended approach to solve the full BDB–NS equations to find out (for a few representative cases) how broadly applicable the predictions coming from the solution of the linearized equations are.

3. Results and discussion

We begin by analysing the results for transverse oscillations of first circular and then elliptical cylinders. Before we proceed, it is useful to remember that the magnitude of the (real) force experienced by the cylinder can be written as

$$\begin{aligned}\tilde{F} &= |\tilde{\boldsymbol{F}}| = |\mathrm{Re}(\boldsymbol{F}\mathrm{e}^{\mathrm{i}\tilde{t}})| = |F|\sin(\tilde{t}-\phi)\\ &= |F|\cos\phi\sin\tilde{t} - |F|\sin\phi\cos\tilde{t} = \pi\mathcal{R}(C_e^t\sin\tilde{t} - C_d^t\cos\tilde{t}),\end{aligned} \tag{3.1}$$

where ϕ is the phase lag between the force and prescribed displacement $\tilde{y}=\sin\tilde{t}$. The average power required to sustain the vibrations in one period can then be calculated as

$$\tilde{\mathcal{P}} = \frac{1}{2\pi}\int_0^{2\pi}\tilde{\boldsymbol{F}}\cdot\tilde{\boldsymbol{u}}_c\,\mathrm{d}\tilde{t} = -\frac{\pi}{2}\mathcal{R}C_d^t. \tag{3.2}$$

Equation (3.2) highlights the fact that the average power consumption is directly proportional to the damping coefficient.

Figure 3(*a*,*b*) shows the variations of the effective mass and damping coefficients of a circular cylinder as a function of $\delta=\beta/\sqrt{\mathcal{R}}$ for different values of the dimensionless frequency $\mathcal{R}$. The parameter δ represents the ratio of two length scales, namely the oscillation penetration length that scales with $1/\sqrt{\mathcal{R}}$ and the characteristic permeation length that scales with $1/\beta$ (see e.g. Vainshtein & Shapiro 2009). Dashed lines in the insets are plots of the asymptotic expressions for the corresponding coefficients in the limits of high/low oscillation frequency and permeability (see table 1 in appendix A). The behaviour of the dimensionless force magnitude and phase shift between the force and prescribed displacement (see (3.1)) associated with the plots of C_e^t and C_d^t are shown in figures 3(*c*) and 3(*d*), respectively.

Inspecting figure 3(*a*), we see that the curves for the effective mass coefficient all start as a nearly horizontal line when the permeability is very low ($\delta\gg 1$). With an increase in the permeability, as one might intuitively expect, C_e^t begins to decay. This trend continues as C_e^t asymptotically approaches zero with a rate that is proportional to δ^4 (see table 1 in appendix A). The rapid decay in the magnitude of the effective mass coefficient is due to two factors (see (3.1)): (i) the monotonic decrease of the force magnitude with increasing permeability, as depicted in figure 3(*c*); and (ii) the rise of the phase lag to $\pi/2$ at high permeabilities (see figure 3*d*). Each of these factors has a δ^2 contribution to the overall decay rate of C_e^t.

Similar to the effective mass plots, the curves for the damping coefficient plateau in the zero-permeability limit (see figure 3*b*). However, unlike those plots, when

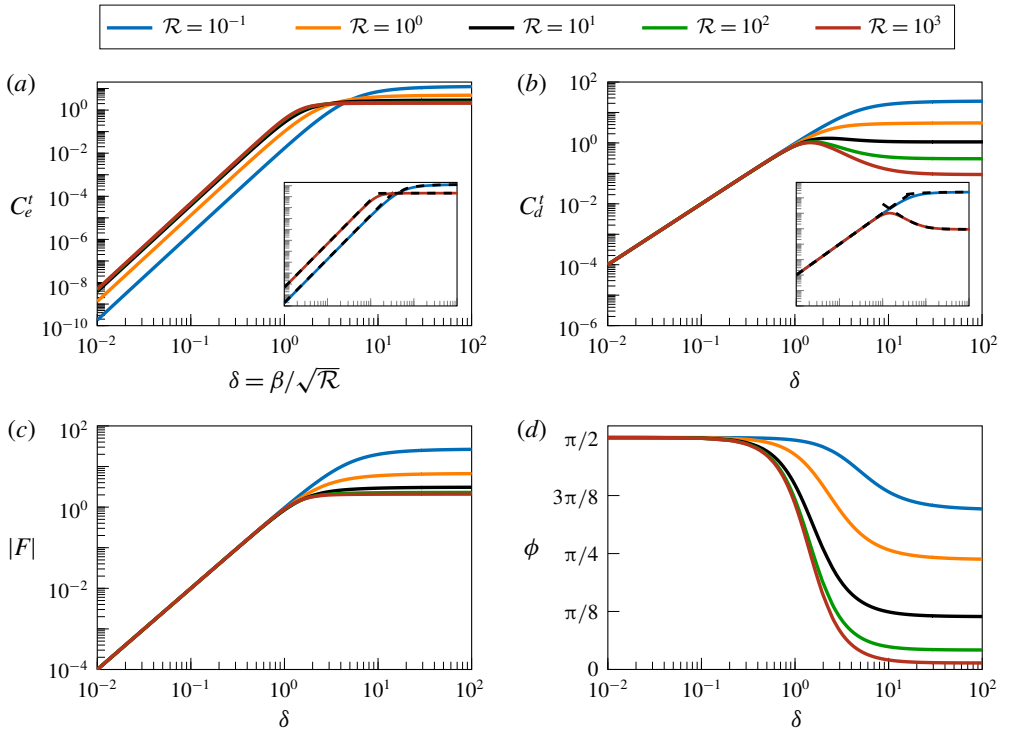

FIGURE 3. (Colour online) Dimensionless (*a*) effective mass and (*b*) damping coefficients of a transversely oscillating porous circular cylinder as a function of $\delta = \beta/\sqrt{\mathcal{R}}$ for different values of the dimensionless frequency $\mathcal{R}$. Dashed lines in the insets are plots of the asymptotic expressions in the limits of high/low oscillation frequency and permeability (see table 1 in appendix A). Dimensionless (*c*) force magnitude and (*d*) phase shift between the force and prescribed displacement associated with the plots in (*a*) and (*b*) (see (3.1)).

the oscillation frequency is not too low, C_d^t initially increases on increasing the permeability from nil, reaches a maximum and then approaches zero as the permeability tends to infinity (see figure 3*b*). In this limit, all curves converge to a single line of slope δ^2 (see also table 1 in appendix A). The existence of a maximum in C_d^t at moderate to high frequencies suggests that, in these regimes, the increase in $\sin\phi$ initially outweighs the drop in $|F|$ and, by doing so, yields a greater damping coefficient (see (3.1)). This trend reverses, of course, as the permeability continues to increase. Evidently, the maximum C_d^t seems always to occur at $\delta \sim O(1)$. Perhaps even more intriguing, the maximum C_d^t, depending on the frequency, may be many times greater than the damping coefficient of the impermeable cylinder $C_{d,\infty}^t$. For instance, at $\mathcal{R} = 10^3$, the ratio $C_{d,max}^t/C_{d,\infty}^t$ is approximately 11.2, whereas it is close to 3.8 for $\mathcal{R} = 10^2$ (see figure 3*b*). Interestingly, the reduction in C_e^t, on the other hand, is not typically as pronounced as the increase in C_d^e at low permeabilities. For example, at $\mathcal{R} = 10^3$ and $\delta = 3$, $C_d^t/C_{d,\infty}^t = 5.66$ and $C_e^t/C_{e,\infty}^t = 0.92$ or, at $\mathcal{R} = 10^2$ and $\delta = 3$, $C_d^t/C_{d,\infty}^t = 2.39$ and $C_e^t/C_{e,\infty}^t = 0.85$.

Next, we consider transverse oscillations of elliptical cylinders in the direction of their minor axes. The results are presented in figure 4. Here, the cylinder's semi-major

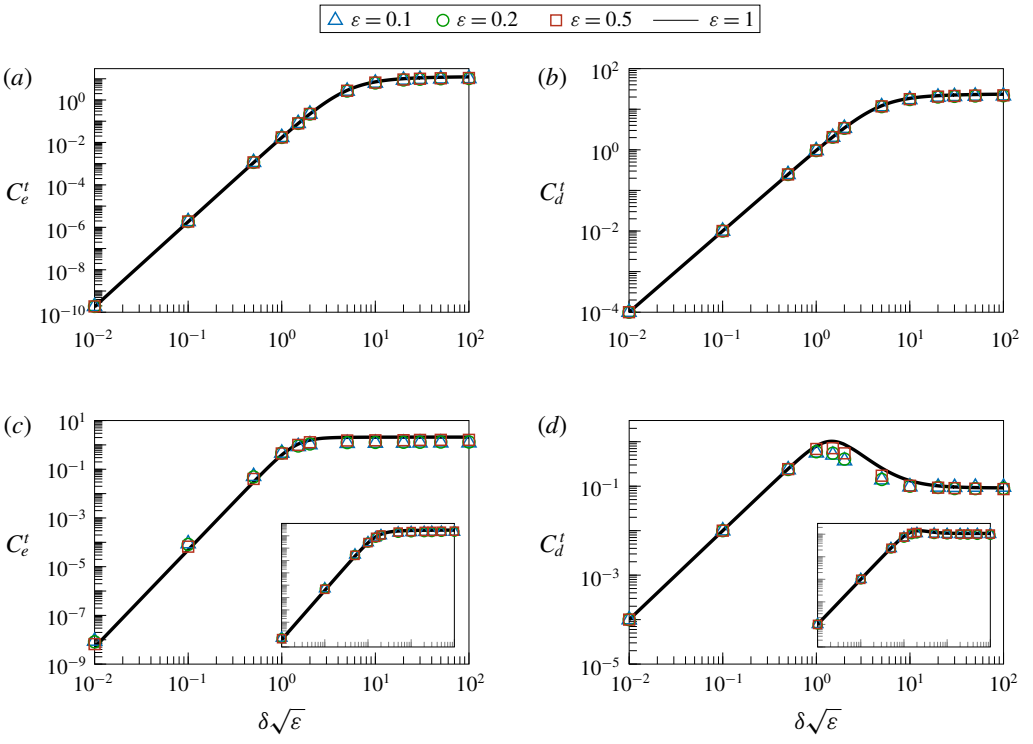

FIGURE 4. (Colour online) Dimensionless (*a*,*c*) effective mass and (*b*,*d*) damping coefficients of transversely oscillating porous elliptical cylinders of various aspect ratio ε. The dimensionless frequency is $\mathcal{R} = 10^{-1}$ in (*a*,*b*), and $\mathcal{R} = 10^3$ in the primary plots and $\mathcal{R} = 10$ in the insets of (*c*,*d*). The results are plotted versus the modified δ, i.e. δ multiplied by $\sqrt{\varepsilon}$.

axis is chosen as its characteristic length a and the ratio of the cylinder's minor to major axis (its aspect ratio) is denoted by ε. More importantly, the coefficients are plotted versus $\delta\sqrt{\varepsilon}$ (the modified δ). Multiplying δ with $\sqrt{\varepsilon}$ is equivalent to redefining the dimensionless permeability as $\beta^2 = ab/\kappa$ (see Masoud, Stone & Shelley 2013), where a and b represent the semi-major and semi-minor axes of the cross-section, respectively. Remember that the original definition is $\beta^2 = a^2/\kappa$. We find that, when the effect of inertia is weak ($\mathcal{R} \ll 1$), the plots for various aspect ratios nearly collapse onto a single master curve and, hence, are very well represented by the analytical results for a circular cylinder (i.e. solid black lines in figure 4(*a*,*b*)). As the frequency of the oscillations increases, deviations from a perfect collapse of data begin to appear (see figure 4(*c*,*d*) and their insets). Mismatches in the C_d^t plots are mainly limited to the range $0.5 \leqslant \delta \leqslant 10$, whereas the deviations in the C_e^t curves are more widespread, particularly at very large $\mathcal{R}$. Overall, from figure 4, we learn that, if adjusted properly, the closed-form expressions derived in § 2.2 for the effective mass and damping coefficients of transversely oscillating circular cylinders can be used to obtain very good estimates for the coefficients of similarly vibrating elliptical cylinders over a broad span of conditions.

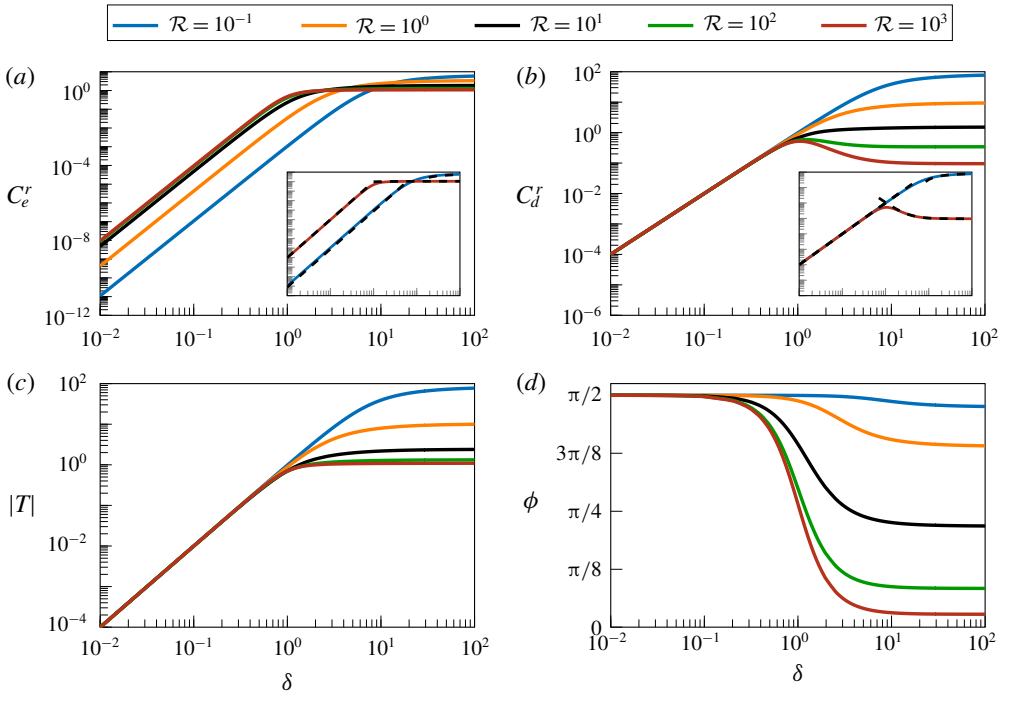

FIGURE 5. (Colour online) Dimensionless (*a*) effective mass and (*b*) damping coefficients of a rotationally oscillating porous circular cylinder as a function of $\delta = \beta/\sqrt{\mathcal{R}}$ for different values of the dimensionless frequency $\mathcal{R}$. Dashed lines in the insets are plots of the asymptotic expressions in the limits of high/low oscillation frequency and permeability (see table 1 in appendix A). (*c*) Dimensionless torque magnitude and (*d*) phase shift between the torque and prescribed angular displacement associated with the plots in (*a*) and (*b*) (see (3.3)).

Having discussed the transverse oscillations, we now examine rotational vibrations. Again, it is constructive to recall that

$$\begin{aligned}\tilde{T} &= |\tilde{\boldsymbol{T}}| = |\mathrm{Re}(\boldsymbol{T}\mathrm{e}^{\mathrm{i}\tilde{t}})| = |T|\sin(\tilde{t}-\phi)\\ &= |T|\cos\phi\sin\tilde{t} - |T|\sin\phi\cos\tilde{t} = \pi\mathcal{R}R_g^2(C_e^r\sin\tilde{t} - C_d^r\cos\tilde{t}),\end{aligned} \tag{3.3}$$

$$\tilde{\mathcal{P}} = \frac{1}{2\pi}\int_0^{2\pi}\tilde{\boldsymbol{T}}\cdot\tilde{\boldsymbol{\Omega}}_c\,\mathrm{d}\tilde{t} = -\frac{\pi}{2}\mathcal{R}R_g^2C_d^r, \tag{3.4}$$

where $\tilde{\boldsymbol{\Omega}}_c = \cos\tilde{t}\,\boldsymbol{e}_z$ is the angular velocity of the cylinder. The results for circular and elliptical cylinders are presented, respectively, in figures 5 and 6, whose formats are identical to those of figures 3 and 4, in that order. As can be seen in these figures, the plots for C_e^r and C_d^r exhibit many of the same features as those for C_e^t and C_d^t, chief among which are the existence of a maximum in the C_d^r curves when inertial effects are dominant and the overall decay of the coefficients with increasing permeability. Despite close qualitative similarities, there are of course quantitative differences. Most notably, at the same $\mathcal{R}$, the ratio $C_{d,max}^r/C_{d,\infty}^r$ is almost half of $C_{d,max}^t/C_{d,\infty}^t$, and δ corresponding to $C_{d,max}^t$ is shifted towards one.

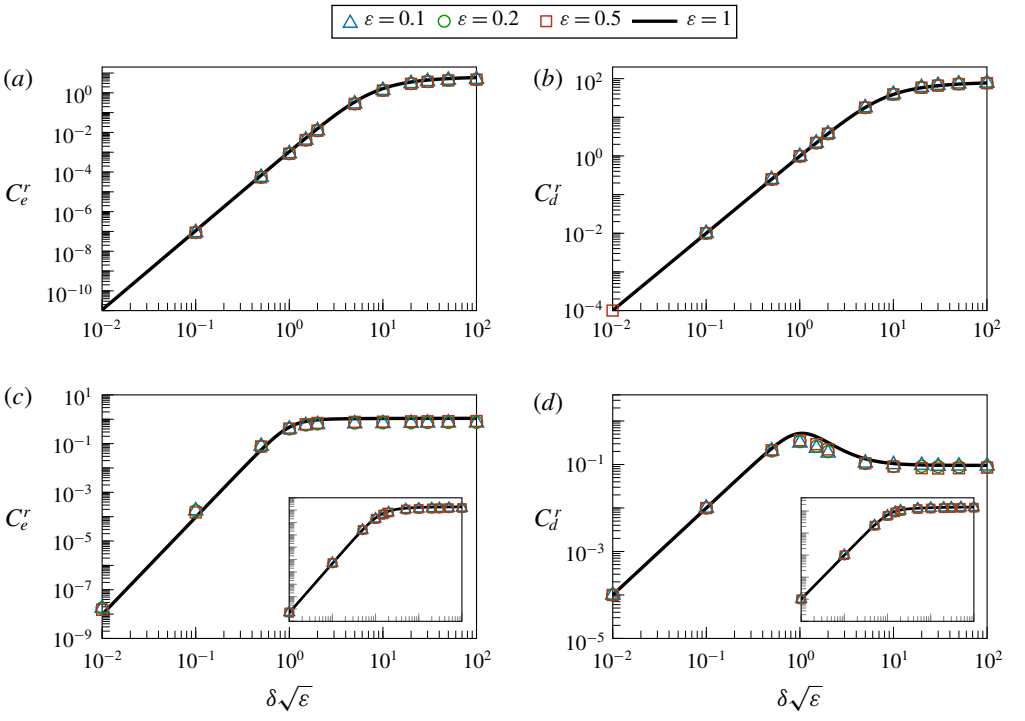

FIGURE 6. (Colour online) Dimensionless (*a*,*c*) effective mass and (*b*,*d*) damping coefficients of rotationally oscillating porous elliptical cylinders of various aspect ratio ε. The dimensionless frequency is $\mathcal{R} = 10^{-1}$ in (*a*,*b*), and $\mathcal{R} = 10^3$ in the primary plots and $\mathcal{R} = 10$ in the insets of (*c*,*d*).

A natural question that may present itself at this point is: How do the behaviour of the effective mass and damping coefficients for vibrating cylinders compare with those for an oscillating sphere? To answer this question, we have analytically solved for C_e^t, C_d^t, C_e^r and C_d^r of a sphere using the method of § 2.2. The derivation details along with the plots of the coefficients versus δ (see figure 8) are presented in appendix B. To the best of our knowledge, these results have not been reported correctly or at all elsewhere. The comparison of figures 3 and 5 against figure 8 reveals that there is a strong resemblance between the behaviour of the effective mass and damping coefficients of cylinders and spheres. It also indicates that the critical dimensionless frequency $\mathcal{R}_c$, beyond which the damping coefficient maximizes at a finite δ, is higher for a sphere than it is for a circular cylinder. In addition, we observe that, at a given $\mathcal{R} > \mathcal{R}_c$, the ratios $C_{d,max}^t/C_{d,\infty}^t$ and $C_{d,max}^r/C_{d,\infty}^r$ for a sphere are roughly 35 % and 20 % less than their counterparts for a circular cylinder, respectively.

In concluding this section, we examine the validity of the small-amplitude assumption under which the presented results were obtained. Figure 7 shows the percentage difference between the results of full and linearized NS calculations for the damping coefficient of finite-amplitude transverse and rotational oscillations. The results are shown for two representative cross-sections, circular and elliptical with aspect ratio $\varepsilon = 0.1$, and for the highest frequency considered in this study, i.e. $\mathcal{R} = 10^3$, where the largest deviations from the small-amplitude theory are expected

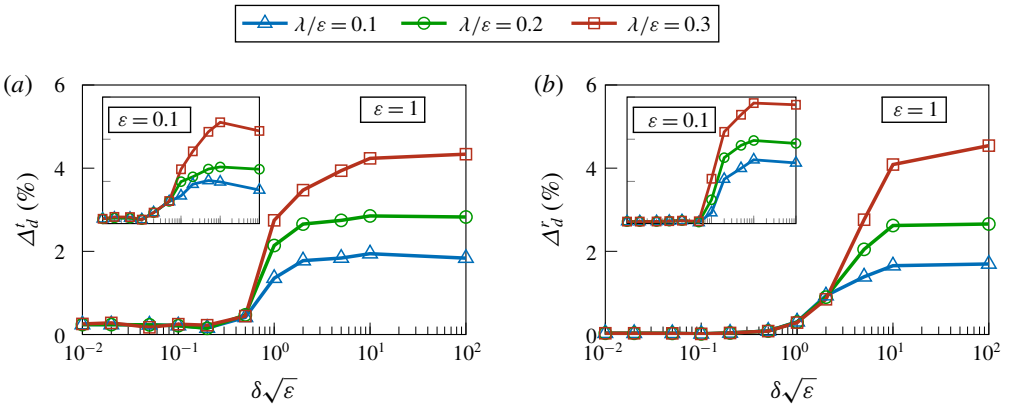

FIGURE 7. (Colour online) Percentage difference between the results of full and linearized NS calculations for the damping coefficients of porous cylinders oscillating (*a*) transversely and (*b*) rotationally with finite amplitudes. The primary plots belong to circular cylinders, whereas those in the insets are for elliptical cylinders of aspect ratio $\varepsilon = 0.1$. The dimensionless frequency is $\mathcal{R} = 10^3$ in all plots.

to occur. When the cross-section is circular ($\varepsilon = 1$), we see that the difference stays below 5 % for the dimensionless amplitude as high as $\lambda = 0.3$, which indicates how wide the applicability range of the small-amplitude assumption can be. For the same ratio of the amplitude to aspect ratio (i.e. $\lambda/\varepsilon = 0.3$), we see that the difference is similarly low (less than 6 %) for the elliptical cross-section of $\varepsilon = 0.1$. That an error of similar magnitude is reached at a lower amplitude for $\varepsilon = 0.1$, compared to $\varepsilon = 1$, is due to the more vigorous vortex shedding from the sharp edges as the cross-section gets thinner. This nonlinear phenomenon is not captured by the linearized model.

4. Conclusion

We systematically investigated the dynamic response of fluid-submerged porous (circular and elliptical) cylinders under periodic (transverse and rotational) oscillations of small amplitude. Using analytical and numerical modelling, we demonstrated how the oscillation frequency and permeability affect the hydrodynamic performance of cylinders characterized by their effective mass and damping coefficients. Perhaps surprisingly, we discovered that, at high enough oscillation frequencies, permeable cylinders can significantly outperform their impermeable counterparts when used as dampers to dissipate oscillatory mechanical energy. What is intriguing is that, in those cases, a drastic change in the damping characteristics of impermeable cylinders can be achieved by making them slightly permeable. Our calculations indicate that the optimal damping occurs when the ratio of the characteristic length of oscillation penetration and the characteristic permeation length is of order one. This and other findings of our study can serve as engineering guidelines for designing porous damping structures with superior hydrodynamic performance, which may be used, for example, as stabilizers in deep-water offshore platforms to dampen unwanted environmental disturbances. We also hope that the insights gained by our analyses guide and/or motivate future theoretical and experimental investigations on the subject. Potentially interesting directions to pursue are considering other geometries,

	$\delta \to 0$ $\mathcal{R} \to 0$	$\delta \to 0$ $\mathcal{R} \to \infty$	$\delta \to \infty$ $\mathcal{R} \to 0$	$\delta \to \infty$ $\mathcal{R} \to \infty$
C_e^t	$\frac{\pi}{16}\mathcal{R}\delta^4$	$\frac{\delta^4}{2}$	$\frac{1}{\Gamma}\left(\frac{\pi}{\mathcal{R}} + 2\Lambda - 1 + \frac{\pi^2}{8} + \frac{2\pi\Lambda}{\mathcal{R}^{3/2}\Gamma\delta}\right)$	$2\left(1 + \sqrt{\frac{2}{\mathcal{R}}} - \frac{2}{\sqrt{\mathcal{R}}\delta}\right)$
C_d^t	δ^2	δ^2	$\frac{1}{\Gamma}\left[-\frac{4\Lambda}{\mathcal{R}} + \frac{\pi}{2}\left(1 - \frac{\Lambda}{\Gamma}\right) + \frac{4\Gamma - 8\Lambda^2}{\mathcal{R}^{3/2}\Gamma\delta}\right]$	$2\left(\sqrt{\frac{2}{\mathcal{R}}} + \frac{1}{\mathcal{R}} + \frac{2}{\delta^2}\right)$
C_e^r	$-\frac{\Lambda}{16}\mathcal{R}^2\delta^4$	δ^4	$1 - 4\Lambda + \frac{16\Lambda}{\sqrt{\mathcal{R}}\delta}$	$1 + 2\sqrt{\frac{2}{\mathcal{R}}} - \frac{4}{\sqrt{\mathcal{R}}\delta}$
C_d^r	δ^2	δ^2	$\frac{8}{\mathcal{R}} + \pi - \frac{16}{\mathcal{R}^{3/2}\delta}$	$2\sqrt{\frac{2}{\mathcal{R}}} + \frac{6}{\mathcal{R}} + \frac{1}{\delta^2}$

TABLE 1. Asymptotic expressions for the effective mass and damping coefficients of transversely and rotationally oscillating porous circular cylinders. The new parameters Λ and Γ are defined as $\Lambda = \ln(\sqrt{\mathcal{R}}/2) + \Upsilon$ and $\Gamma = \Lambda^2 + \pi^2/16$, where Υ is the Euler constant.

large-amplitude oscillations and confinement effects. Performing pore-resolved numerical simulations would be well worth while, too.

Acknowledgements

We thank M. Aureli for stimulating discussions. This research was carried out in part using the computational resources provided by the Superior high-performance computing facility at Michigan Technological University.

Appendix A. Asymptotic expressions for the effective mass and damping coefficients of circular cylinders

The expressions derived for the effective mass and damping coefficients of circular cylinders in § 2.2 involve modified Bessel functions of complex arguments. To make the intricate calculations more accessible and to gain additional physical insights, in table 1 we present simplified formulae for the effective mass and damping coefficients of circular cylinders in the asymptotic limits of high/low oscillation frequency and permeability. Several considerations are made in deriving the asymptotic expressions. First, in the two limits involving $\delta \to 0$, only the largest non-zero terms are retained (see the top two rows of table 1). Second, in the limit $\delta \to \infty$ and $\mathcal{R} \to 0$, we demand that $\beta = \delta\sqrt{\mathcal{R}} \to \infty$. This additional restriction is not needed in the opposite limit $\delta \to 0$ and $\mathcal{R} \to \infty$, because, in that situation, the magnitude of ξ_i goes to infinity irrespective of whether $\delta\sqrt{\mathcal{R}}$ is finite, decays to zero or blows up (see (2.5)). Third, when $\delta \to \infty$ and $\mathcal{R} \to \infty$, it is assumed that δ and $\sqrt{\mathcal{R}}$ increase at about the same rate. Lastly, in cases where $\delta \to \infty$, we keep the largest terms involving δ (i.e. the leading-order corrections due to the permeability of the cylinder) and δ-independent terms of the same or greater order of magnitude (see the bottom two rows of table 1).

Appendix B. Small-amplitude oscillations of a porous sphere

The solution approach adopted in § 2.2 to solve for the flow field within and around a vibrating porous circular cylinder can also be used to derive closed-form expressions for the velocity distribution in the interior and exterior of an oscillating porous sphere of radius a when the amplitude of oscillations is small relative to a. To proceed with the derivations, we need to first determine the fundamental singularities of the BDB equations for three-dimensional internal and external flows. The three-dimensional equivalents of stokeson, potential doubleton and roton, and of stokeslet, potential doublet and rotlet (see § 2.2 for the name convention) can be shown to be, respectively (see also Pozrikidis 1989),

$$\boldsymbol{u}_{SN}(\boldsymbol{r};\boldsymbol{\alpha}) = \frac{(\rho_i^2+1)\sinh\rho_i-\rho_i\cosh\rho_i}{\rho_i^3}\left[\boldsymbol{\alpha}-\frac{3\xi_i^2(\boldsymbol{\alpha}\cdot\boldsymbol{r})\boldsymbol{r}}{\rho_i^2}\right]+\frac{2\xi_i^2\sinh\rho_i(\boldsymbol{\alpha}\cdot\boldsymbol{r})\boldsymbol{r}}{\rho_i^3}, \tag{B 1a}$$

$$p_{SN}(\boldsymbol{r};\boldsymbol{\alpha}) = 0, \tag{B 1b}$$

$$\boldsymbol{u}_{DN}(\boldsymbol{r};\boldsymbol{\eta}) = \boldsymbol{\eta}, \tag{B 2a}$$

$$p_{DN}(\boldsymbol{r};\boldsymbol{\eta}) = -\xi_i^2(\boldsymbol{\eta}\cdot\boldsymbol{r}), \tag{B 2b}$$

$$\boldsymbol{u}_{RN}(\boldsymbol{r};\boldsymbol{\gamma}) = \frac{\rho_i\cosh\rho_i-\sinh\rho_i}{\rho_i^3}(\boldsymbol{\gamma}\times\boldsymbol{r}), \tag{B 3a}$$

$$p_{RN}(\boldsymbol{r};\boldsymbol{\gamma}) = 0, \tag{B 3b}$$

$$\boldsymbol{u}_S(\boldsymbol{r};\boldsymbol{\alpha}) = 2\left[\mathrm{e}^{-\rho_o}\left(1+\frac{1}{\rho_o}+\frac{1}{\rho_o^2}\right)-\frac{1}{\rho_o^2}\right]\frac{\boldsymbol{\alpha}}{r} - 2\left[\mathrm{e}^{-\rho_o}\left(1+\frac{3}{\rho_o}+\frac{3}{\rho_o^2}\right)-\frac{3}{\rho_o^2}\right]\frac{(\boldsymbol{\alpha}\cdot\boldsymbol{r})\boldsymbol{r}}{r^3}, \tag{B 4a}$$

$$p_S(\boldsymbol{r};\boldsymbol{\alpha}) = \frac{2(\boldsymbol{\alpha}\cdot\boldsymbol{r})}{r^3}, \tag{B 4b}$$

$$\boldsymbol{u}_D(\boldsymbol{r};\boldsymbol{\eta}) = -\mathrm{e}^{-\rho_o}(1+\rho_o+\rho_o^2)\left[\frac{\boldsymbol{\eta}}{r^3}-\frac{3(\boldsymbol{\eta}\cdot\boldsymbol{r})\boldsymbol{r}}{r^5}\right]-\frac{2\mathrm{e}^{-\rho_o}\rho_o^2(\boldsymbol{\eta}\cdot\boldsymbol{r})\boldsymbol{r}}{r^5}, \tag{B 5a}$$

$$p_D(\boldsymbol{r};\boldsymbol{\eta}) = 0, \tag{B 5b}$$

$$\boldsymbol{u}_R(\boldsymbol{r};\boldsymbol{\gamma}) = \frac{2\mathrm{e}^{-\rho_o}(\rho_o+1)}{r^3}(\boldsymbol{\gamma}\times\boldsymbol{r}), \tag{B 6a}$$

$$p_R(\boldsymbol{r};\boldsymbol{\gamma}) = 0. \tag{B 6b}$$

As explained in § 2.2, for the translational oscillations, the velocity and pressure fields take the forms of

$$\boldsymbol{u}_i = \boldsymbol{u}_{SN}(\boldsymbol{r};\alpha_i\boldsymbol{e}_y)+\boldsymbol{u}_{DN}(\boldsymbol{r};\eta_i\boldsymbol{e}_y)+(\beta/\xi_i)^2\boldsymbol{e}_y, \tag{B 7a}$$

$$p_i = p_{SN}(\boldsymbol{r};\alpha_i\boldsymbol{e}_y)+p_{DN}(\boldsymbol{r};\eta_i\boldsymbol{e}_y), \tag{B 7b}$$

$$\boldsymbol{u}_o = \boldsymbol{u}_S(\boldsymbol{r};\alpha_o\boldsymbol{e}_y)+\boldsymbol{u}_D(\boldsymbol{r};\eta_o\boldsymbol{e}_y), \tag{B 8a}$$

$$p_o = p_S(\boldsymbol{r};\alpha_o\boldsymbol{e}_y)+p_D(\boldsymbol{r};\eta_o\boldsymbol{e}_y), \tag{B 8b}$$

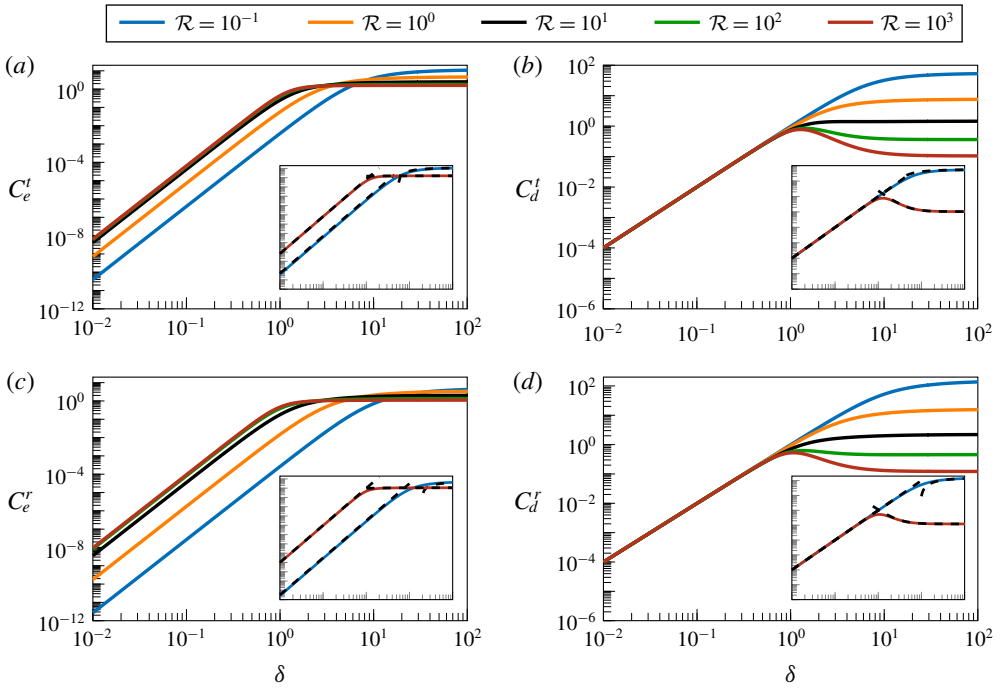

FIGURE 8. (Colour online) Dimensionless (*a*,*c*) effective mass and (*b*,*d*) damping coefficients of (*a*,*b*) transversely and (*c*,*d*) rotationally oscillating porous spheres as a function of $\delta = \beta/\sqrt{\mathcal{R}}$ for different values of the dimensionless frequency $\mathcal{R}$. Dashed lines in the insets are plots of the asymptotic expressions in the limits of high/low oscillation frequency and permeability (see table 2).

where, upon the application of the continuity boundary conditions at $r = 1$, the unknown coefficients are found to be

$$\alpha_i = \frac{A_3}{A_2}, \quad \eta_i = -\frac{\beta^2}{\xi_i^2}\left(1 - \frac{A_1}{A_2}\right), \quad \alpha_o = \frac{\beta^2}{2}\left(1 - \frac{A_1}{A_2}\right), \quad \eta_o = \frac{\beta^2}{\xi_o^2}\left(1 - \frac{A_1 + A_4}{A_2}\right), \tag{B 9a–d}$$

with

$$A_1 = 2\xi_i^4(\xi_i \cosh \xi_i + \xi_o \sinh \xi_i), \tag{B 10a}$$

$$A_2 = \cosh \xi_i[3\beta^2\xi_i(\xi_o + 1) + \xi_i^3\xi_o^2 + 2\xi_i^5] + \sinh \xi_i[-3\beta^2(\xi_o + 1) + \xi_i^2\xi_o^3 + 2\xi_i^4\xi_0], \tag{B 10b}$$

$$A_3 = -3\beta^2\xi_i^3(\xi_o + 1), \tag{B 10c}$$

$$A_4 = 3\xi_i^2 e^{\xi_o}(\xi_i \cosh \xi_i - \sinh \xi_i). \tag{B 10d}$$

It then follows that

$$\boldsymbol{F} = \beta^2 \int_S (\boldsymbol{u}_i - \boldsymbol{u}_c)\, \mathrm{d}S = \frac{4\pi}{3}\frac{\beta^2}{\xi_i^2}\left[\frac{2\alpha_i}{\xi_i}(\xi_i \cosh \xi_i - \sinh \xi_i) + \eta_i \xi_i^2 - \mathrm{i}\mathcal{R}\right]\boldsymbol{e}_y. \tag{B 11}$$

	$\delta \to 0$ $\mathcal{R} \to 0$	$\delta \to 0$ $\mathcal{R} \to \infty$	$\delta \to \infty$ $\mathcal{R} \to 0$	$\delta \to \infty$ $\mathcal{R} \to \infty$
C_e^t	$\frac{\sqrt{2}}{9}\mathcal{R}^{3/2}\delta^4$	$\frac{2}{3}\delta^4$	$\frac{3}{2}\left(1+\frac{3}{\sqrt{2\mathcal{R}}}-\frac{3\sqrt{2}}{\mathcal{R}\delta}\right)$	$\frac{3}{2}\left(1+\frac{3}{\sqrt{2\mathcal{R}}}-\frac{3}{\sqrt{\mathcal{R}\delta}}\right)$
C_d^t	δ^2	δ^2	$\frac{9}{2}\left(\frac{1}{\sqrt{2\mathcal{R}}}+\frac{1}{\mathcal{R}}-\frac{1}{\mathcal{R}^{3/2}\delta}\right)$	$\frac{9}{2}\left(\frac{1}{\sqrt{2\mathcal{R}}}+\frac{1}{\mathcal{R}}+\frac{1}{2\delta^2}\right)$
C_e^r	$\frac{1}{32}\mathcal{R}^2\delta^4$	δ^4	$6-5\sqrt{\frac{\mathcal{R}}{2}}-\frac{30}{\sqrt{\mathcal{R}\delta}}$	$1+\frac{5}{\sqrt{2\mathcal{R}}}-\frac{5}{\sqrt{R\delta}}$
C_d^r	δ^2	δ^2	$5\left(\frac{3}{\mathcal{R}}+\sqrt{\frac{\mathcal{R}}{2}}-\frac{9}{\mathcal{R}^{3/2}\delta}\right)$	$\frac{5}{\sqrt{2\mathcal{R}}}+\frac{10}{\mathcal{R}}+\frac{1}{\delta^2}$

TABLE 2. Asymptotic expressions for the effective mass and damping coefficients of transversely and rotationally oscillating porous spheres.

Again per § 2.2, the flow field for the rotational vibrations is expressed as

$$\boldsymbol{u}_i = \boldsymbol{u}_{RN}(\boldsymbol{r};\gamma_i\boldsymbol{e}_z) + (\beta/\xi_i)^2(\boldsymbol{e}_z\times\boldsymbol{r}), \tag{B 12a}$$

$$p_i = p_{RN}(\boldsymbol{r};\gamma_i\boldsymbol{e}_z), \tag{B 12b}$$

$$\boldsymbol{u}_o = \boldsymbol{u}_R(\boldsymbol{r};\gamma_o\boldsymbol{e}_z), \tag{B 13a}$$

$$p_o = p_R(\boldsymbol{r};\gamma_o\boldsymbol{e}_z), \tag{B 13b}$$

where

$$\gamma_i = \frac{-\beta^2\xi_i(\xi_o^2+3\xi_o+3)}{\beta^2\sinh\xi_i+\xi_i\xi_o(\xi_o\cosh\xi_i+\xi_i\sinh\xi_i)}, \tag{B 14a}$$

$$\gamma_o = \frac{\beta^2 e^{\xi_o}[(\xi_i^2+3)\sinh\xi_i-3\xi_i\cosh\xi_i]}{2\xi_i^2[\beta^2\sinh\xi_i+\xi_i\xi_o(\xi_o\cosh\xi_i+\xi_i\sinh\xi_i)]}. \tag{B 14b}$$

Hence, the torque exerted on the sphere is

$$\boldsymbol{T}=\beta^2\int_S[\boldsymbol{r}\times(\boldsymbol{u}_i-\boldsymbol{u}_c)]\,\mathrm{d}S=\frac{8\pi}{3}\frac{\beta^2}{\xi_i^2}\left\{\frac{\gamma_i}{\xi_i^3}[(\xi_i^2+3)\sinh\xi_i-3\xi_i\cosh\xi_i]-\frac{\mathrm{i}\mathcal{R}}{5}\right\}\boldsymbol{e}_z. \tag{B 15}$$

The corresponding effective mass and damping coefficients are obtained by substituting F and T from above into

$$C_e^t=-\mathrm{Im}[F/(4\pi\mathcal{R}/3)] \quad\text{and}\quad C_d^t=-\mathrm{Re}[F/(4\pi\mathcal{R}/3)], \tag{B 16a,b}$$

$$C_e^r=-\mathrm{Im}[T/(4\pi\mathcal{R}R_g^2/3)] \quad\text{and}\quad C_d^r=-\mathrm{Re}[T/(4\pi\mathcal{R}R_g^2/3)], \tag{B 17a,b}$$

where

$$R_g^2=\frac{\int_V(x^2+y^2)\,\mathrm{d}V}{\int_V\mathrm{d}V}. \tag{B 18}$$

Figure 8 shows the variations of C_e^t, C_d^t, C_e^r and C_d^r versus δ for various $\mathcal{R}$. The figure is supplemented by table 2, which presents simple expressions justifying the behaviour of the plots in the asymptotic limits of low/high δ and $\mathcal{R}$. The formulae are obtained subject to the same considerations as in appendix A.

REFERENCES

ABRAMOWITZ, M. & STEGUN, I. A. 1972 *Handbook of Mathematical Functions: with Formulas, Graphs, and Mathematical Tables*. Dover.

AHSAN, S. N. & AURELI, M. 2015 Finite amplitude oscillations of flanged laminas in viscous flows: vortex–structure interactions for hydrodynamic damping control. *J. Fluids Struct.* **59**, 297–315.

AN, S. & FALTINSEN, O. M. 2013 An experimental and numerical study of heave added mass and damping of horizontally submerged and perforated rectangular plates. *J. Fluids Struct.* **39**, 87–101.

AVUDAINAYAGAM, A. & GEETHA, J. 1994 Oscillatory Stokes flow in two dimensions. *Mech. Res. Commun.* **21** (6), 617–628.

BARTA, E. 2011 Motion of slender bodies in unsteady Stokes flow. *J. Fluid Mech.* **688**, 66–87.

BRINKMAN, H. C. 1947 A calculation of the viscous force exerted by a flowing fluid on a dense swarm of particles. *Appl. Sci. Res.* A **1**, 27–34.

BRINKMAN, H. C. 1948 On the permeability of media consisting of closely packed porous particles. *Appl. Sci. Res.* A **1**, 81–86.

CHWANG, A. T. & WU, T. Y.-T. 1975 Hydromechanics of low-Reynolds-number flow. Part 2. Singularity method for Stokes flows. *J. Fluid Mech.* **67** (4), 787–815.

DEBYE, P. & BUECHE, A. M. 1948 Intrinsic viscosity, diffusion, and sedimentation rate of polymers in solution. *J. Chem. Phys.* **16**, 573–579.

FELDERHOF, B. U. 2014 Velocity relaxation of a porous sphere immersed in a viscous incompressible fluid. *J. Chem. Phys.* **140** (13), 134901.

GRAHAM, D. R. & HIGDON, J. J. L. 2002 Oscillatory forcing of flow through porous media. Part 2. Unsteady flow. *J. Fluid Mech.* **465**, 237–260.

KANWAL, R. P. 1955 Vibrations of an elliptic cylinder and a flat plate in a viscous fluid. *Z. Angew. Math. Mech.* **35** (1-2), 17–22.

KANWAL, R. P. 1964 Drag on an axially symmetric body vibrating slowly along its axis in a viscous fluid. *J. Fluid Mech.* **19** (4), 631–636.

KANWAL, R. P. 1970 Note on slow rotation or rotary oscillation of axisymmetric bodies in hydrodynamics and magnetohydrodynamics. *J. Fluid Mech.* **41** (4), 721–726.

KOLOMENSKIY, D. & SCHNEIDER, K. 2009 A Fourier spectral method for the Navier–Stokes equations with volume penalization for moving solid obstacles. *J. Comput. Phys.* **228** (16), 5687–5709.

LAI, R. Y. S. & MOCKROS, L. F. 1972 The Stokes-flow drag on prolate and oblate spheroids during axial translatory accelerations. *J. Fluid Mech.* **52** (1), 1–15.

LAWRENCE, C. J. & WEINBAUM, S. 1986 The force on an axisymmetric body in linearized, time-dependent motion: a new memory term. *J. Fluid Mech.* **171**, 209–218.

LAWRENCE, C. J. & WEINBAUM, S. 1988 The unsteady force on a body at low Reynolds number; the axisymmetric motion of a spheroid. *J. Fluid Mech.* **189**, 463–489.

LIU, Y., LI, H.-J., LI, Y.-C. & HE, S.-Y. 2011 A new approximate analytic solution for water wave scattering by a submerged horizontal porous disk. *Appl. Ocean Res.* **33** (4), 286–296.

LOEWENBERG, M. 1993 The unsteady Stokes resistance of arbitrarily oriented, finite-length cylinders. *Phys. Fluids* **5** (11), 3004–3006.

LOOKER, J. R. & CARNIE, S. L. 2004 The hydrodynamics of an oscillating porous sphere. *Phys. Fluids* **16** (1), 62–72.

MASOUD, H., STONE, H. A. & SHELLEY, M. J. 2013 On the rotation of porous ellipsoids in simple shear flows. *J. Fluid Mech.* **733**, R6.

MOLIN, B. 2001 On the added mass and damping of periodic arrays of fully or partially porous disks. *J. Fluids Struct.* **15** (2), 275–290.

MOLIN, B. 2011 Hydrodynamic modeling of perforated structures. *Appl. Ocean Res.* **33** (1), 1–11.

OLLILA, S. T. T., ALA-NISSILA, T. & DENNISTON, C. 2012 Hydrodynamic forces on steady and oscillating porous particles. *J. Fluid Mech.* **709**, 123–148.

PHAN, C. N., AURELI, M. & PORFIRI, M. 2013 Finite amplitude vibrations of cantilevers of rectangular cross sections in viscous fluids. *J. Fluids Struct.* **40**, 52–69.

POZRIKIDIS, C. 1989 A singularity method for unsteady linearized flow. *Phys. Fluids* **1** (9), 1508–1520.

POZRIKIDIS, C. 1992 *Boundary Integral and Singularity Methods for Linearized Viscous Flow*. Cambridge University Press.

POZRIKIDIS, C. 2011 *Introduction to Theoretical and Computational Fluid Dynamics*. Oxford University Press.

PRAKASH, J., RAJA SEKHAR, G. P. & KOHR, M. 2012 Faxen's law for arbitrary oscillatory Stokes flow past a porous sphere. *Arch. Mech.* **64** (1), 41–63.

RAY, M. 1936 Vibration of an infinite elliptic cylinder in a viscous liquid. *Z. Angew. Math. Mech.* **16** (2), 99–108.

SADER, J. E. 1998 Frequency response of cantilever beams immersed in viscous fluids with applications to the atomic force microscope. *J. Appl. Phys.* **84** (1), 64–76.

SANTHANAKRISHNAN, A., ROBINSON, A. K., JONES, S., LOW, A. A., GADI, S., HEDRICK, T. L. & MILLER, L. A. 2014 Clap and fling mechanism with interacting porous wings in tiny insect flight. *J. Expl Biol.* **217** (21), 3898–3909.

SHATZ, L. F. 2004 Singularity method for oblate and prolate spheroids in Stokes and linearized oscillatory flow. *Phys. Fluids* **16** (3), 664–677.

SHATZ, L. F. 2005 Slender body method for slender prolate spheroids and hemispheroids on planes in linearized oscillatory flow. *Phys. Fluids* **17** (11), 113603.

SHU, J.-J. & CHWANG, A. T. 2001 Generalized fundamental solutions for unsteady viscous flows. *Phys. Rev.* E **63** (5), 051201.

STOKES, G. G. 1851 On the effect of the internal friction of fluids on the motion of pendulums. *Trans. Camb. Phil. Soc.* **9**, 8–106.

TSAI, C.-C. & HSU, T.-W. 2010 The method of fundamental solutions for oscillatory and porous buoyant flows. *Comput. Fluids* **39** (4), 696–708.

TUCK, E. O. 1969 Calculation of unsteady flows due to small motions of cylinders in a viscous fluid. *J. Engng Maths* **3** (1), 29–44.

VAINSHTEIN, P. & SHAPIRO, M. 2009 Forces on a porous particle in an oscillating flow. *J. Colloid Interface Sci.* **330** (1), 149–155.

WILLIAMS, W. E. 1966 A note on slow vibrations in a viscous fluid. *J. Fluid Mech.* **25** (3), 589–590.

ZHANG, W. & STONE, H. A. 1998 Oscillatory motions of circular disks and nearly spherical particles in viscous flows. *J. Fluid Mech.* **367**, 329–358.